DOI: 10.1002/((please add manuscript number))
Article type: Full Paper

Black Phosphorus Quantum Dots Induced High-Quality Perovskite Film for Efficient and Thermally Stable Planar Perovskite Solar Cells

*Weitao Yang, Jiehuan Chen, Xiaomei Lian, Jun Li, Fenfa Yao, Gang Wu, Weiming Qiu, Chuanhong Jin, Paul Heremans, and Hongzheng Chen**

W. Yang, J. Chen, X. Lian, J. Li, Prof. G. Wu, Prof. H. Chen
State Key Laboratory of Silicon Materials
MOE Key Laboratory of Macromolecular Synthesis and Functionalization
Department of Polymer Science and Engineering
Zhejiang University
Hangzhou 310027, P. R. China
E-mail: hzchen@zju.edu.cn
Dr. W. Qiu, Prof. P. Heremans
IMEC
Kapeldreef 75
Heverlee B-3001, Belgium
Prof. C. Jin, F. Yao
State Key Laboratory of Silicon Materials
School of Materials Science and Engineering
Zhejiang University
Hangzhou 310027, P. R. China

Keywords: black phosphorus quantum dots, perovskite solar cells, trap suppression, crystal quality, device thermal stability

Abstract: Crystallinity and trap-state density of a perovskite film plays a critical role in the performance of corresponding perovskite solar cells (PVSCs). Herein, liquid-phase-exfoliated black phosphorus quantum dots (BPQDs) are incorporated into the perovskite precursor solution as additives to direct the formation of perovskite film, i.e. methylammonium lead iodide ($MAPbI_3$). It is found that the perovskite films made with BPQDs have higher crystallinity and less non-radiative detects compared to the pristine ones, leading to longer carrier lifetime and higher carrier collection efficiency. Time-of-flight secondary-ion mass spectra and surface density calculation of BPQDs reveal that the improvement of perovskite film quality may be related to the heterogeneous nucleation of the perovskite film at the BPQDs. PVSCs using $MAPbI_3$ films made with BPQDs achieve a maximum power conversion efficiency (PCE) of 20.0% and an encouraging thermal stability of T_{80}=100 h at 100°C. Both values are remarkably higher than the devices with pristine perovskite films. Therefore, this work demonstrates the potential of two-dimensional materials quantum dots assisted growth method for high-performance PVSCs.

1. Introduction

Perovskite solar cells (PVSCs) have emerged as promising next generation photovoltaics due to their high power conversion efficiency (PCE) and their compatibility with those solution-processing techniques used for large-area fabrication.[1-8] These metal halide perovskite materials have shown many characteristics that are suitable for solar cell applications, e.g. tunable bandgap, long carrier diffusion length, large carrier mobility, and low exciton binding energy.[3, 9-14] To date, the PCE of the state-of-the-art PVSCs has exceeded 23%. This was achieved primarily by the growth of highly-crystalline and low-defect perovskite films as well as by significant progress in the passivation of device interfaces.[15, 16] In order to acquire high-quality perovskite films, researchers have developed a number of preparation strategies. Among these, the additive-assisted growth method has been widely exploited and shown to be effective.[17-23] For example, Liu and his co-worker have introduced semiconducting molecules with Lewis acid or base functional groups into the perovskite absorber, leading to an improved PCE of 19.3% and better environmental stability.[18] Sulfonic zwitterion was adopted by Huang's group for crystallization control and defect passivation, which resulted in a high PCE of 21.1% for mixed-cations PVSCs.[20] Recently, Huang's group has introduced carbon quantum dots as additive in PVSCs for grain boundary passivation, yielding an improved PCE of 18.24% and better stability.[23]

As an interesting category of materials with many unique optoelectronic properties, two-dimensional (2D) materials, such as MoS_2, graphene oxide (GO), antimonene (Sb), and black phosphorene (BP), have been used to improve the performance of perovskite solar cells, mostly as interfacial buffer layers.[24-30] For instance, Sun et al. adopted GO as hole transport layer (HTL), which could not only facilitate the hole extraction, but also help to form perovskite film with higher coverage and favorable textures.[25] As a result, the GO-based PVSCs outperform those employing PEDOT:PSS as HTL. Similarly, Song *et al.* used Sb nanosheets as extra hole-extraction layer on poly[bis(4-phenyl)(2,4,6-trimethylphenyl)amine] (PTAA) for planar inverted PVSCs.[26] Thanks to suitable energy level and high carrier mobility of Sb nanosheets, the double hole-extraction layer led to an improved PCEs of 20.0% from 17.6%. Since these previous studies certainly indicated such 2D materials could form good interfaces with perovskites, it would be of great interest to investigate the effects of incorporating them into the bulk of perovskite films. BP has also been adopted as charge transport material in PVSCs.[24, 27, 28] Thanks to its suitable energy alignment and high carrier mobility, the PVSCs employing BP as charge transport material offered an increased PCE reaching 16%.[24, 27]

In this work, we employ liquid-phase-exfoliated (LPE) black phosphorus quantum dots (BPQDs) as additives in the perovskite precursor solution to tailor the growth of methylammonium lead iodide ($MAPbI_3$) films. BPQDs are chosen first because of their previously reported superior electronic properties and good compatibility with perovskite.[24, 27, 28] Secondly, the organic perovskite precursors, in this case methylammonium iodide (MAI), are well dissolved in the solvent used for BPQDs suspension, i.e. isopropanol (IPA). Therefore, by using a dynamic two-step interdiffusion method, BPQDs can be easily incorporated into the perovskite film by mixing with the organic precursors.[7] We have found that the BPQDs-assisted processing can lead to $MAPbI_3$ with significantly improved crystallinity and reduced carrier traps. As a result, a superior PCE of 20.0% is achieved for perovskite solar cells using $MAPbI_3$ made with BPQDs additives compared to that using pristine $MAPbI_3$ films. Moreover, the BPQDs-based devices present remarkably improved thermal stability, maintaining over 80% of their initial PCE after intense thermal stress at 100°C for 100h. Therefore, our work indicates the incorporation of 2D materials to perovskite bulk film is a promising route for high-quality perovskite films.

2. Results and Discussion

The LPE BPQDs are characterized by high-resolution TEM (HR-TEM), atomic force microscope (AFM) and Raman spectroscopy. As shown in **Figure 1**a, the lattice fringes derived from the HRTEM image and the corresponding fast Fourier transform pattern (the right-bottom inset image) are consistent, and were determined to be 0.27 nm, 0.34 nm, and 0.43 nm from different BPQDs, which are consistent with the former reports.[24, 31, 32] From the Raman spectra (Figure 1c), three characteristic peaks corresponding to A^1_g, B_{2g}, and A^2_g vibrational modes of BP were detected. Compared to bulk BP, the A^1_g, B_{2g}, and A^2_g modes of BPQDs are blue-shifted by about 1, 1.5 and 2.0 cm^{-1}, respectively, indicating the existence of few-layers.[31, 32] AFM height and phase images of BPQDs are presented in Figure 1c and Figure 1d, respectively. In those images, BPQDs show an average size of 22.4±2.4 nm and a thickness of ~1 nm. BPQDs suspensions in IPA and in DMF were presented in Figure S1. They stay clear and stable during the whole research period (more than 9 month), indicating good compatibility between BPQDs and perovskite. $MAPbI_3$ films with and without BPQDs were then fabricated using the dynamic two-step deposition method and were integrated into PVSCs to study the effect of BPQDs on film formation and device performance. Since IPA was used as solvent for both BPQDs and MAI, mixing of BPQDs was realized by directly adding BPQDs suspension to the MAI solution. The amount of BPQDs were optimized by varying the volume fraction of the BPQDs suspension in the total solution, and the pure IPA solvent that was added to keep the MAI concentration at 50 mg mL^{-1}. The details for device fabrication can be seen in Experimental Section.

The schematics of device structure and energy level diagram are presented in **Figure 2**a and Figure 2b. As shown in Table S1, all the devices with BPQDs exhibit better performance than the reference PVSCs, with the optimal volume fraction determined to be 25%. Therefore, in the following study, we focused on films and devices based on this optimal ratio, which hereafter will be denoted as film or device with BPQDs. The current density-voltage (J-V) curve and external quantum efficiency (EQE) spectrum of the reference device and those of the device with BPQDs are presented in Figure 2c and Figure 2d, with the detailed device parameters listed in **Table 1**. The statistics of PCE distributions and the J-V curves of the best devices scanned from forward and reverse directions are shown in Figure S2. The device with BPQDs shows improved performance with a higher power conversion efficiency (PCE) of 20.0% (an average PCE of 18.7%±0.5%), a FF of 0.83, a J_{sc} of 21.9 mA cm^{-2} and a V_{oc} of 1.10 V. The EQE spectrum depicts an enhancement of EQE in visible range, implying higher carrier collection efficiency with the help of BPQDs. Photocurrent density (J_{ph}) versus effective voltage (V_{int}) under illumination at 100 mW cm^{-2} was examined to depict the charge extraction ability of the devices. J_{ph} is calculated by $J_{ph}=J_L-J_D$, where J_L and J_D are the current density under illumination and in the dark, respectively. V_{int} is calculated by $V_{int}=V_{bi}-V_{applied}$, where V_{bi} is the built-in potential, which refers to the voltage at which J_{ph} is zero, and $V_{applied}$ is the applied voltage. The charge collection probability (Pc) is define as Pc=J_{ph}/J_{sat}, where J_{sat} is the saturated J_{ph} at large enough V_{int}. As shown in Figure 2e, the Pc increases from 94.8% to 95.5% under maximum output condition after adding BPQDs. Higher Pc suggests more carriers are swept out prior to recombination, which agrees with the enhanced photovoltaic performance.[33] Besides, the operating stability of the best BPQDs-based device was examined under applied bias voltage (0.90 V) at the maximum power output point. The steady-state photocurrent and stabilized power output, as shown in Figure 2f, are 21.2 mA cm^{-2} and 19.1%, respectively.

Previous research has revealed the close relation between the $MAPbI_3$ crystal quality and photovoltaic performance of PVSCs. In this case, we also attribute the PCE increase of the BPQDs device to the improved $MAPbI_3$ film formation with the assistance of BPQDs. $MAPbI_3$ films without and with BPQDs were examined via scanning electron microscope (SEM), X-ray diffraction (XRD), and photoluminescence (PL) spectra. As presented in **Figure 3**a,b, the average grain size slightly increases from 170±68 nm to 239±95 nm after adding BPQDs. Detailed grain size distributions of perovskite films with and without BPQDs are presented in Figure S3a in Supporting Information. However, from the XRD patterns (Figure 3c), the diffraction peak at around 14.1°, which is corresponding to the (110) lattice plane of the $MAPbI_3$ crystal, becomes stronger (intensity increases from 3.8×10^5 to 7.6×10^5) after incorporating with BPQDs, indicating the increase in crystallinity.[34] The full width at half maxima of the peak slightly decreases from 0.149° to 0.143°, which agrees well with the enlarged perovskite grain size according to the Scherrer equation. Moreover, although the absorptions of the films with and without BPQDs are identical, the PL intensity of the film with BPQDs is much higher than that of the reference film, suggesting a reduced non-radiative recombination in the film with BPQDs (Figure 3d). To confirm this, we also carried out time-resolved PL (TRPL) to estimate the carrier life time of different perovskite films made on bare glass without any transport layer. As shown in **Figure 4**a, the average τ increases from 78.11 ns (reference film) to 95.57 ns after adding

BPQDs. Therefore, the XRD, PL and TRPL results indicate the BPQDs-assisted process leads to perovskite films with higher crystallinity and lower non-radiative traps.

To further look into the trap state density within perovskite films, we probed the dark current density-voltage (*J*-*V*) characteristics using single-carrier devices. Hole-only devices were made using a structure of ITO/PTAA/perovskite/PTAA/MoO_3/Ag, while the electron-only device used a structure of ITO/SnO_2/ perovskite /PCBM/BCP/Ag. The *J*-*V* curves of these electron-only and hole-only devices based on $MAPbI_3$ films without and with BPQDs are shown in Figure 4b and Figure 4c. In each, we can observe sequentially the Ohmic region (n=1), the trap-filling region and the trap-free space charge limit current (SCLC) region (n=2).[11, 35] In the electron-only condition, trap-filled limit voltages (V_{TFL}) were obtained as 0.22 V and 0.34 V for devices with and without BPQDs, respectively. In the hole-only condition, V_{TFL} were obtain as 0.81 V and 1.04 V for devices with and without BPQDs, respectively. The trap state density was calculated by equation $N_{\mathrm{defects}}=2\varepsilon\varepsilon_0 V_{\mathrm{TFL}}/eL^2$, where ε (= 32) and ε_0 (= 8.85×10^{-12} F m^{-1}) are the relative dielectric constants of $MAPbI_3$ and the vacuum permittivity, respectively, L (≈ 300 nm) is the thickness of the perovskite film, and e (= 1.6×10^{-19} C) is the elementary charge.[11, 35] We found that the trap densities of the electron-only device (and hole-only device) decrease from 1.37×10^{16} cm^{-3} to 8.86×10^{15} cm^{-3} (and from 4.09×10^{16} cm^{-3} to 3.19×10^{16} cm^{-3}) by using the perovskite film with BPQDs, indicating efficient defects suppression after adding BPQDs. These results are in well agreement with the observation from the steady-state PL and TRPL measurements that the incorporation of BPQDs reduce non-radiative recombination.

Electrochemical impedance spectroscopy (EIS) was employed to study the charge carrier behavior within different devices. Figure 4d displays the Cole-Cole plots of the device measured in dark, where a single arc representing the recombination process appeared in low frequence area.[36, 37] The equivalent circuit was shown in the top right inset. In this circuit, R_s represents the Ohmic resistance of the electrodes and bulk and R_{rec} is related to the recombination resistance. Therefore, a much larger R_{rec} of the device with BPQDs (12.6 kΩ) than the reference device (6.5 kΩ) originates from the higher quality perovskite film as well as the superior electronic properties of BPQDs, indicating effective suppression of charge recombination, which attributes to improved FF (Table 1).

Time-of-flight secondary-ion mass spectrometry (SIMS) was carried out to further investigate the distribution of BPQDs in the perovskite film. Here, I_2^-, InO^- signals were adopted to define the boundary of perovskite film and ITO/glass substrate, respectively, while PO_3^- signal was adopted to trace the distribution of BPQDs. As shown in Figure 4e, the PO_3^- signal emerges after the I_2^- signal but before the InO^- signal, implying that BPQDs tend to distribute at the bottom of perovskite film. Considering the bottom-up growth of the two-step-prepared perovskite film, as well as good compatibility and potential interaction between BPQDs and perovskite, we assume that BPQDs might serve as heterogeneous nucleation centers, because of which they would enrich at the bottom of the perovskite layer.[24, 27] To explain the improvements in crystallinity upon addition of BPQDs, we assess whether the density of BPQDs can be correlated with the density of crystal grains of $MAPbI_3$. Assuming that a single BPQD is a round disc with diameter (*φ*) of 22.4 nm and thickness (*d*) of 1 nm, the surface density (σ) of the BPQDs in perovskite films could be estimated by : $\sigma = cL/\rho V_m$, where c (≈ 0.010 mg mL^{-1}) is the concentration of BPQDs in IPA solutions, L (≈ 300 nm) is the thickness of the perovskite film, ρ (= 2.70 g cm^{-3}) is the density of black phosphorus, and V_m is the volume of a single BPQD sphere. The surface density σ of BPQDs is then: $\sigma = 2.8\times10^{8}$ cm^{-2}, giving an average inter-QD spacing of $D = (1/\sigma)^{0.5} = 597$ nm. This spacing is expected to be equal to the grain size of perovskite film when the nucleation of $MAPbI_3$ would be solely triggered by BPQDs. From Figure 3a,b we observe that the average grain size of the $MAPbI_3$ film with BPQDs (239 nm) is between 587 nm (the average QD spacing) and 170 nm (the average grain size of the pristine $MAPbI_3$ film), and hence suggest that BPQDs-assisted heterogeneous nucleation rivals the homogeneous nucleation during the crystallization of perovskite films. Detailed calculations and discussion could be found in Equations (S1), (S2) in the Supporting Information. Larger grain sizes for the perovskite films with lower concentrations of BPQDs were also observed (Figure S3b), offering further evidence for the nucleation effect of BPQDs. Based on these results, we suggest that BPQDs serve as heterogeneous nucleation centers during the solvent-processing crystallization of $MAPbI_3$, leading to high-quality perovskite film with higher crystallinity and better suppressed defects (illustrated in Figure 4f).

Stability of PVSCs is one of the key issues for the commercial application of PVSCs. Therefore, we also examined the stability of the reference device and the one with BPQDs. Firstly, we tested the thermal stability of the unsealed device by placing different devices on 100°C hotplate in glovebox with continuously heating. PCE degradation of PVSCs under thermal stress has been an intrinsic limitation of the overall device stability, though encapsulation could to some extent slow down the degradation by preventing the outgoing of volatile species from the devices.[38-40] As implied by the normalized PCE evolution (**Figure 5**a), most of the reference devices failed after aging for 24 hours, retaining an average PCE of less than 40% of the initial one. On the contrary, the device with BPQDs exhibited superior thermal stability, keeping over 80% of its initial PCE after aging for 100 hours. To diagnose such deterioration of PCE, we first examed composition change of the perovskite films via XRD and XPS mesurements. As shown in Figure S4a, rather moderate PbI_2 signal was detected after thermal aging for both reference device and BPQDs-doped device. The XPS spectra of Pb 4f and I 3d also show negligible change after thermal aging (Figure S4b-e), indicating no redox reaction of Pb^{2+} and I^-. These results suggest that decomposition of $MAPbI_3$ might not the main reason for the PCE decline under heating in inert atmosphere. Next, perovskite film morphology after thermal aging was studied via SEM characterization. As shown in Figure 5b-e, after thermal annealing at 100°C in glovebox for 50 h, the perovskite film without BPQDs suffered from severe destruction, while negligible changes were found in the perovskite film with BPQDs. Such destruction of $MAPbI_3$ layer would lead to increased bulk resistance, and then decreased FF, which agree well with the normalized FF evolutions shown in Figure S5c. Considering the relatively high thermal expansion coefficient (α_V=1.57×10^{-4} K^{-1}, which is 6 times higher than that of soda lime glass) of $MAPbI_3$ perovskite, we ascribe the destruction of $MAPbI_3$ perovskite film to the strain caused by mismatched α_v of perovskite films and substrate under rather high temperature, expecially in the case of planar structure PVSCs.[41, 42] Therefore, we attribute such improved thermal stability to the stronger $MAPbI_3$-BPQDs grain with high crystallinity, as well as possible stress concerntration effect of BPQDs at the bottom of $MAPbI_3$ film that could alleviate the strain-induced grain break. In addition to the thermal stability, storage stability of the unsealed PVSCs under various humidity conditions were also tested. As shown in Figure S6, the device with BPQDs remained almost 100% of its initial PCE after 240 h storage in ambience with relative humidity (RH) of 25%, and 66% of the initial PCE after stored in a higher humidity of RH=50% for another 240 h. It is worth to note that the reference device without BPQDs exhibits similar humidity stability, and we speculate this is possibly because the device degradation in this case is more related to interface layers.

3. Conclusion

In conclusion, we have developed a BPQDs-assisted processing method to achieve perovskite films with higher crystallinity, larger grain size and lower non-radiative defect density. Concentrated distribution of P element at the bottom of perovskite film was observed via SIMS measurement, suggesting that BPQDs may serve as heterogeneous nucleation centers during the perovskite film formation. The use of perovskite films with BPQDs leads to significantly improved device performance, reaching a PCE of 20%. In addition, the mechanical stability of PVSC under thermal aging is significantly enhanced, keeping over 80% of of its initial PCE after aging for 100 hours at 100°C. Therefore, this work demonstrates the beneficial effects of incorporating 2D materials quantum dots into the bulk of perovskite films and will trigger the interest in exploring novel additive-assisted growth method and 2D materials/perovskite composites for highly performing perovskite solar cells.

4. Experimental Section

Materials: Dimethyl sulfoxide (DMSO), N,N-dimethylformamide (DMF), PbI_2 were purchased from TCI. Chlorobenzene (CB), ethanol, isopropanol (IPA), and toluene were bought from Sigma Aldrich. 15% SnO_2 colloid solution in water was acquired from Alfa Aesar. Bathocuproine (BCP), [6,6]-phenyl-C61-butyric acid methyl ester (PCBM), Poly[bis(4-phenyl)(2,4,6-trimethylphenyl)amine] (PTAA) were obtained from J&K., American Dye Source and Xi'an p-OLED, respectively. Methylammonium iodide (MAI) was purchased from Shanghai Mater Win New Materials. All materials were used without further purification.

Exfoliation of BP: 10 mg of BP crystal (99.998%, purchased from XianFengnano) was first ground, and then dispersed in 10 mL of IPA, followed by ultrasonication with a power of 700 W for 20 h. The dispersion was centrifuged at 12k revolutions per minute (rpm) for 30 min to collect the supernatant. The concentration of BPNFs suspension is determined to be ~0.010 mg mL^{-2} by collecting and weighing the BPNFs product from certain volume of suspension. Picture of the BPQDs in IPA and in DMF are presented in Figure. S1.

Device Fabrication and characterization: Perovskite solar cells were fabricated on glass substrates pre-coated with a layer of indium tin oxides (ITO), using a device structure of ITO/PTAA/perovskite/PCBM/BCP/Ag. The ITO substrates were cleaned sequentially by detergent, deionized water, acetone, and isopropanol for 15 min in an ultrasonic bath before fabrication. The pre-cleaned ITO substrates were then treated with UV-Ozone for 20 min. To deposit the PTAA layer, the ITO substrates were transferred to a glovebox. Then a layer of PTAA (2 mg mL^{-1} in toluene) was spin-coated onto the cleaned ITO at 6000 rpm for 45 s. PbI_2(DMSO) was dissolved in DMF at a concentration of 1 M. For the pure MAI solution, MAI was dissolved in IPA at a concentration of 50 mg mL^{-1}. For the MAI solution with BPQDs, various volumes of BPQDs suspension in IPA were mixed with MAI solution, but the final MAI concentration is kept at 50 mg mL^{-1}. To make the perovskite film, the PbI_2(DMSO) solution was spin coted onto the PTAA film at 3000 rpm for 30s, immediately followed by spin coating of MAI solution or BPQDs-mixed MAI solution at 3000 rpm for another 30 s. Afterward, the obtained film were annealed at 95°C for 15 min. PCBM solution (20 mg mL^{-1} in CB) was then spin-coated on the perovskite film at 2000 rpm for 30 s, followed by the spin-coating of a BCP solution (0.5 mg mL^{-1} in ethanol) at 3000 rpm for 30 s. After this, the samples were transfer to the vacuum chamber for the deposition of 100 nm Ag under a high vacuum of 5×10^{-4} Pa.

Electron-only devices were made using a structure of ITO/SnO_2/perovskite/PCBM/BCP/Ag. To deposit the SnO_2 layer, 15% SnO_2 colloid solution was diluted by deionized water to 5% and thereafter spun coat onto ITO substrates at 3500 rpm for 45s, followed by thermal annealing in air at 150°C for 30 min. The rest layers were deposited in the same way as for the solar cells.

The X-ray diffraction patterns were recorded at a scan rate of 10° min^{-1} on Rigaku Ultima IV X-ray diffractometer with Cu Kα radiation (0.15406 nm). The UV–vis absorption spectra were taken on UV-2450 UV-Vis Shimadzu Spectrophotometer. The field-emission scanning electron microscope (FESEM) measurements were carried out on Hitachi S-4800 machine. The current density-voltage (*J-V*) curves of the devices were measured in glovebox with Keithley 2400 measurement source units under 1 sun, AM 1.5 G spectra from a solar simulator (Taiwan, Enlitech), and the light intensity was calibrated with a standard silicon photovoltaic reference cell. The voltage step is 0.02 V, with a delay time of 10 ms per step, the total scanning rate is 0.095 V s^{-1}.The external quantum efficiency (EQE) spectra were measured by a Solar Cell Spectral Response Measurement System QE-R3011 (Enlitech, Taiwan). For devices storage stability test, devices were stored in a chamber with controlled temperature and humidity. During the aging period, the devices were taken into the glovebox from time to time for PCE decay tracing. For devices thermal stability test, devices were placed on 100 °C hotplate in glovebox. During the aging period, the devices were taken off the hotplate and cooled to room temperature from time to time for PCE decay tracing. The time-of-flight secondary-ion mass spectrometry (SIMS) were conducted on a TOF.SIMS V instrument (Ion-TOF, GmbH, Germany). Dual beam depth profiling used a pulsed 30 keV Bi_3^+ liquid metal ion gun as a primary ion source and a 10 keV Argon gas cluster ion beam with the beam current being adjusted to 1 nA as a sputtering ion source in an interlaced mode. At first, the sputter beam was used to sputter the sample surface for 10 s (or 20 s) to clean possible contamination on the sample surface during sample preparation. Then, data were collected until the ITO/glass substrate was reached as indicated by the increase in the InO^- ion intensity. The analysis area was 100 × 100 μm^2 in the centerof a crater of 300 × 300 μm^2. A low energy flood gun with the beam current of 3.6 μA was used for charge compensation during analysis.

The electrochemical impedance spectroscopy (EIS) was measured with an M204 Multi-Channel Autolab Cabinet in the frequency range of 100 Hz to 1 MHz with a 20 mV perturbation under 0 V bias in the dark.

Characterization of BPQDs: The high-resolution TEM (HR-TEM) images were taken on JEM-2100F at 200 kV accelerating voltage. The Raman spectra were collected using a Renishaw inVia System with a 532 nm laser at 2 mW power. The atomic force microscopy (AFM) images were taken on a Veeco Multimode atomic force microscope in the tapping mode.

Supporting Information

Supporting Information is available from the Wiley Online Library or from the author.

Acknowledgements

This work was supported by the National Natural Science Foundation of China (Grant Nos. 51620105006 and 61721005), Zhejiang Province Science and Technology Key Plan (No. 2018C01047), and International Science and Technology Cooperation Program of China (ISTCP) (Grant No. 2016YFE0102900). W. Qiu would like to thank the financial support of postdoctoral grant from the Research Fund Flanders (FWO).

Received: ((will be filled in by the editorial staff))
Revised: ((will be filled in by the editorial staff))
Published online: ((will be filled in by the editorial staff))

References

[1] J. Huang, Y. Yuan, Y. Shao, Y. Yan, *Nat. Rev. Mater.* **2017**, *2*, 17042.

[2] Y. Deng, X. Zheng, Y. Bai, Q. Wang, J. Zhao, J. Huang, *Nat. Energy* **2018**, *3*, 560.

[3] H. J. Snaith, *Nat. Mater.* **2018**, *17*, 372.

[4] Y. Wu, X. Yang, W. Chen, Y. Yue, M. Cai, F. Xie, E. Bi, A. Islam, L. Han, *Nat. Energy* **2016**, *1*, 16148.

[5] A. Kojima, K. Teshima, Y. Shirai, T. Miyasaka, *J. Am. Chem. Soc.* **2009**, *131*, 6050.

[6] H. Tan, A. Jain, O. Voznyy, X. Lan, F. P. García de Arquer, J. Z. Fan, R. Quintero-Bermudez, M. Yuan, B. Zhang, Y. Zhao, F. Fan, P. Li, L. N. Quan, Y. Zhao, Z.-H. Lu, Z. Yang, S. Hoogland, E. H. Sargent, *Science* **2017**, *355*, 722.

[7] C. Huang, W. Fu, C.-Z. Li, Z. Zhang, W. Qiu, M. Shi, P. Heremans, A. K. Y. Jen, H. Chen, *J. Am. Chem. Soc.* **2016**, *138*, 2528.

[8] G. Yang, C. Chen, F. Yao, Z. Chen, Q. Zhang, X. Zheng, J. Ma, H. Lei, P. Qin, L. Xiong, W. Ke, G. Li, Y. Yan, G. Fang, *Adv. Mater.* **2018**, *30*, 1706023.

[9] S. D. Stranks, G. E. Eperon, G. Grancini, C. Menelaou, M. J. P. Alcocer, T. Leijtens, L. M. Herz, A. Petrozza, H. J. Snaith, *Science* **2013**, *342*, 341.

[10] F. Hao, C. C. Stoumpos, R. P. H. Chang, M. G. Kanatzidis, *J. Am. Chem. Soc.* **2014**, *136*, 8094.

[11] Q. Dong, Y. Fang, Y. Shao, P. Mulligan, J. Qiu, L. Cao, J. Huang, *Science* **2015**, *347*, 967.

[12] Y. Zhisheng, Y. Ligong, W. Gang, W. Mang, C. Hongzheng, *Acta Chim. Sin.* **2011**, *69*, 627.

[13] T. Ye, W. Fu, J. Wu, Z. Yu, X. Jin, H. Chen, H. Li, *J. Mater. Chem. A* **2016**, *4*, 1214.

[14] P.-L. Qin, G. Yang, Z.-w. Ren, S. H. Cheung, S. K. So, L. Chen, J. Hao, J. Hou, G. Li, *Adv. Mater.* **2018**, *30*, 1706126.

[15] W. S. Yang, B.-W. Park, E. H. Jung, N. J. Jeon, Y. C. Kim, D. U. Lee, S. S. Shin, J. Seo, E. K. Kim, J. H. Noh, S. I. Seok, *Science* **2017**, *356*, 1376.

[16] N. J. Jeon, H. Na, E. H. Jung, T.-Y. Yang, Y. G. Lee, G. Kim, H.-W. Shin, S. Il Seok, J. Lee, J. Seo, *Nat. Energy* **2018**, *3*, 682.

[17] X. Zheng, B. Chen, J. Dai, Y. Fang, Y. Bai, Y. Lin, H. Wei, Xiao C. Zeng, J. Huang, *Nat. Energy* **2017**, *2*, 17102.

[18] T. Niu, J. Lu, R. Munir, J. Li, D. Barrit, X. Zhang, H. Hu, Z. Yang, A. Amassian, K. Zhao, S. Liu, *Adv. Mater.* **2018**, *30*, 1706576.

[19] J. C. Yu, S. Badgujar, E. D. Jung, V. K. Singh, D. W. Kim, J. Gierschner, E. Lee, Y. S. Kim, S. Cho, M. S. Kwon, M. H. Song, *Adv. Mater.* **2018**, e1805554.

[20] X. Zheng, Y. Deng, B. Chen, H. Wei, X. Xiao, Y. Fang, Y. Lin, Z. Yu, Y. Liu, Q. Wang, J. Huang, *Adv. Mater.* **2018**, *30*, 1803428.

[21] X. Lian, J. Chen, R. Fu, T.-K. Lau, Y. Zhang, G. Wu, X. Lu, Y. Fang, D. Yang, H. Chen, *J. Mater. Chem. A* **2018**, *6*, 24633.

[22] X. Zhang, G. Wu, W. Fu, M. Qin, W. Yang, J. Yan, Z. Zhang, X. Lu, H. Chen, *Adv. Energy Mater.* **2018**, *8*, 1702498.

[23] Y. Ma, H. Zhang, Y. Zhang, R. Hu, M. Jiang, R. Zhang, H. Lv, J. Tian, L. Chu, J. Zhang, Q. Xue, H.-L. Yip, R. Xia, X.a. Li, W. Huang, *ACS Appl. Mater. Interfaces* **2019**, *11*, 3044.

[24] W. Chen, K. Li, Y. Wang, X. Feng, Z. Liao, Q. Su, X. Lin, Z. He, *J. Phys. Chem. Lett.* **2017**, *8*, 591.

[25] F. Zhang, J. He, Y. Xiang, K. Zheng, B. Xue, S. Ye, X. Peng, Y. Hao, J. Lian, P. Zeng, J. Qu, J. Song, *Adv. Mater.* **2018**, *30*, 1803244.

[26] E. Jokar, Z.Y. Huang, S. Narra, C.-Y. Wang, V. Kattoor, C.-C. Chung, E.W.-G. Diau, *Adv. Energy Mater.* **2018**, *8*, 1701640.

[27] N. Fu, C. Huang, P. Lin, M. Zhu, T. Li, M. Ye, S. Lin, G. Zhang, J. Du, C. Liu, B. Xu, D. Wang, S. Ke, *J. Mater. Chem. A* **2018**, *6*, 8886-8894.

[28] M. Batmunkh, K. Vimalanathan, C. Wu, A. S. R. Bati, L. Yu, S. A. Tawfik, M. J. Ford, T. J. Macdonald, C. L. Raston, S. Priya, C. T. Gibson, J. G. Shapter, *Small Methods* **2019**, 1800521.

[29] X. Yang, W. Fu, W. Liu, J. Hong, Y. Cai, C. Jin, M. Xu, H. Wang, D. Yang, H. Chen, *J. Mater. Chem. A* **2014**, *2*, 7727.

[30] X. Yang, W. Liu, M. Xiong, Y. Zhang, T. Liang, J. Yang, M. Xu, J. Ye, H. Chen, *J. Mater. Chem. A* **2014**, *2*, 14798.

[31] Z. Guo, H. Zhang, S. Lu, Z. Wang, S. Tang, J. Shao, Z. Sun, H. Xie, H. Wang, X. F. Yu, *Adv. Funct. Mater.* **2015**, *25*, 6996.

[32] M. Batmunkh, M. Bat-Erdene, J. G. Shapter, *Adv. Energy Mater.* **2018**, *8*, 1701832.

[33] H. Chen, W. Fu, C. Huang, Z. Zhang, S. Li, F. Ding, M. Shi, C.-Z. Li, A. K.-Y. Jen, H. Chen, *Adv. Energy Mater.* **2017**, *7*, 1700012.

[34] L. Zuo, Z. Gu, T. Ye, W. Fu, G. Wu, H. Li, H. Chen, *J. Am. Chem. Soc.* **2015**, *137*, 2674.

[35] J. Chen, L. Zuo, Y. Zhang, X. Lian, W. Fu, J. Yan, J. Li, G. Wu, C.-Z. Li, H. Chen, *Adv. Energy Mater.* **2018**, *8*, 1800438.

[36] J. Jiang, Q. Wang, Z. Jin, X. Zhang, J. Lei, H. Bin, Z.G. Zhang, Y. Li, S. Liu, *Adv. Energy Mater.* **2018**, *8*, 1701757.

[37] V. Gonzalez-Pedro, E.J. Juarez-Perez, W.-S. Arsyad, E.M. Barea, F. Fabregat-Santiago, I. Mora-Sero, J. Bisquert, *Nano Lett.* **2014**, *14*, 888.

[38] W. Li, H. Dong, L. Wang, N. Li, X. Guo, J. Li, Y. Qiu, *J. Mater. Chem. A* **2014**, *2*, 13587.

[39] M. Zhang, S. Dai, S. Chandrabose, K. Chen, K. Liu, M. Qin, X. Lu, J.M. Hodgkiss, H. Zhou, X. Zhan, *J. Am. Chem. Soc.* **2018**, *140*, 14938.

[40] K.O. Brinkmann, J. Zhao, N. Pourdavoud, T. Becker, T. Hu, S. Olthof, K. Meerholz, L. Hoffmann, T. Gahlmann, R. Heiderhoff, M.F. Oszajca, N.A. Luechinger, D. Rogalla, Y. Chen, B. Cheng, T. Riedl, *Nat. Commun.* **2017**, *8*, 13938.

[41] R. Chen, J. Cao, Y. Duan, Y. Hui, T.T. Chuong, D. Ou, F. Han, F. Cheng, X. Huang, B. Wu, N. Zheng, *J. Am. Chem. Soc.* **2019**, *141*, 541.

[42] J.C. Yu, S. Badgujar, E.D. Jung, V.K. Singh, D.W. Kim, J. Gierschner, E. Lee, Y.S. Kim, S. Cho, M.S. Kwon, M.H. Song, *Adv. Mater.* **2019**, *31*, 1805554.

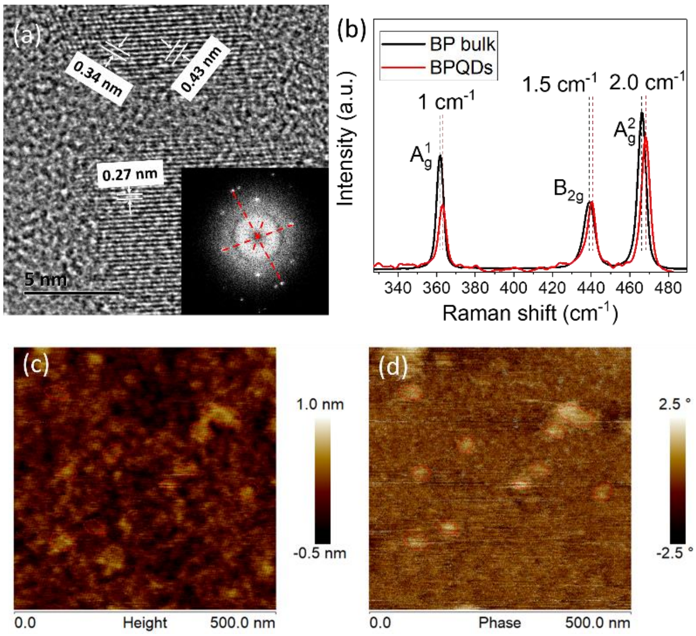

Figure 1. (a) HR-TEM images of BPQDs. Inset is the fast Fourier transform pattern of the image. (b) Raman spectra of BPQDs and bulk BP. AFM (c) height images and (d) phase images of BPQDs on Si substrate. The BPQDs show thickness of ~1 nm, and size of 22.4±2.4 nm.

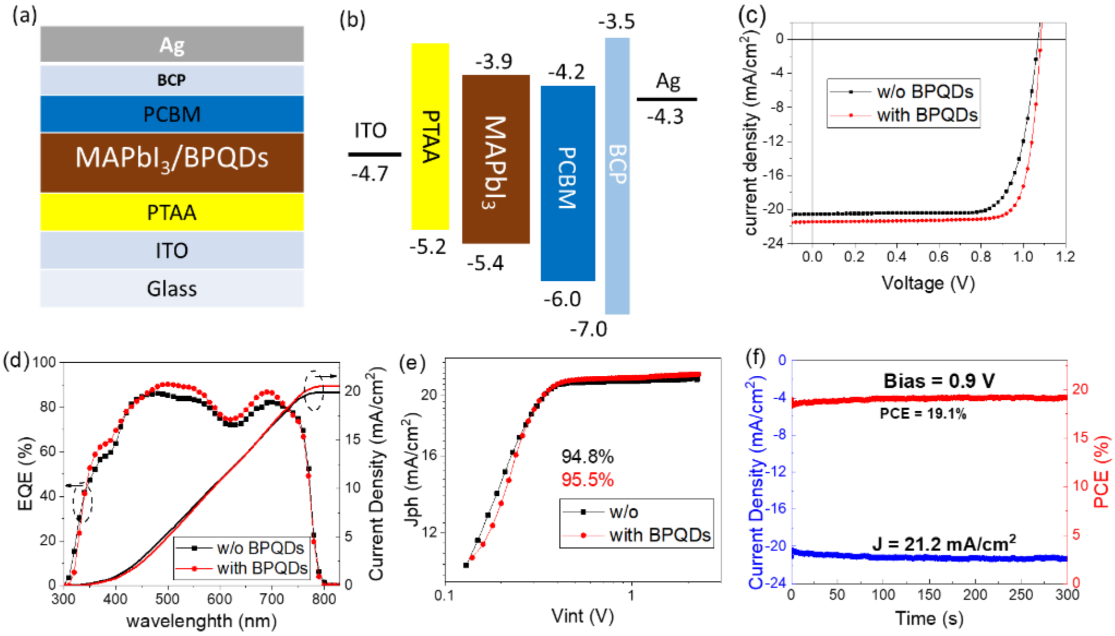

Figure 2. a) Device structure and b) energy level of the adopted perovskite solar cells. c) *J-V* curves and d) EQE spectra of different devices under 1 sun illumination. e) J_{ph} versus V_{int} plots for devices with (red line) and without (black line) BPQDs. f) The steady-state photocurrent measured at a bias voltage (0.90 V) near the maximum power point and the corresponding stabilized power output.

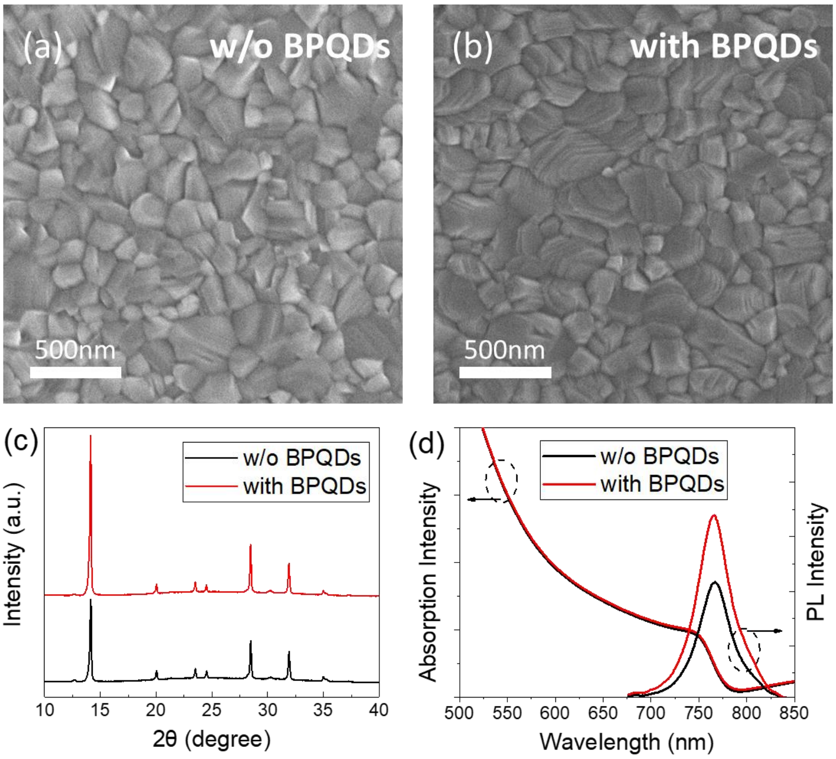

Figure 3. Top-view SEM images of perovskite film a) without and b) with BPQDs. c) Corresponding XRD patterns of the perovskite films on ITO/PTAA substrate. d) Absorption spectra and steady-state PL emission spectra of different perovskite films on bare glass substrate.

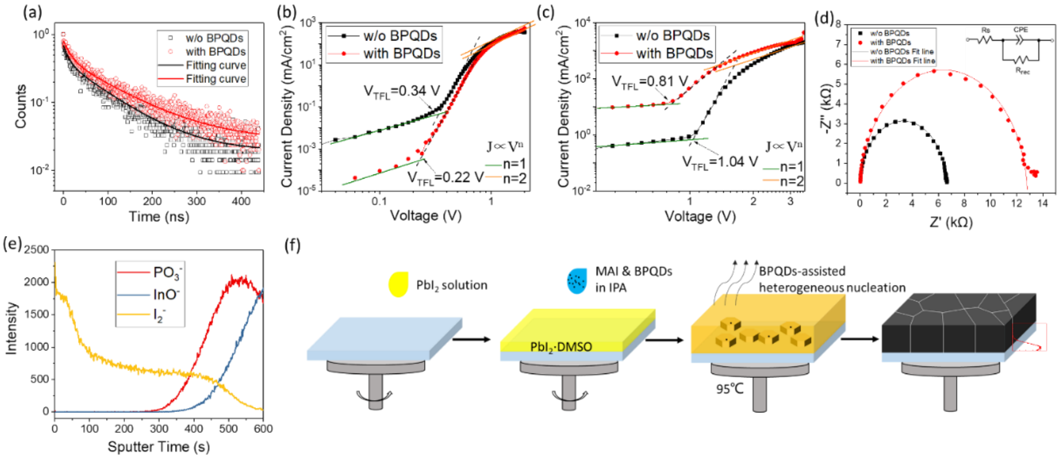

Figure 4. (a) TRPL measurements of perovskite films, the fitting curves are obtained by fitting the data using a bi-exponential rate law. (b) *J-V* characteristics of devices with ITO/SnO_2/ perovskite/PCBM/BCP/Ag configuration utilized for estimating the defect density for perovskite films with and without BPQDs. (c) *J-V* characteristics of devices with ITO/PTAA/ perovskite /PTAA/MoO_3/Ag configuration utilized for estimating the defect density for perovskite films with and without BPQDs. (d) Cole-Cole plots of devices under different conditions. Inset is an equivalent circuit employed in fitting different impedance curves. (e) SIMS profile showing PO_3^-, InO^-,

I_2^- signals from the top of BPQDs-doped perovskite film to the bottom. (f) Scheme of the BPQDs-assisted heterogeneous nucleation process during BPQDs-doped perovskite film preparation.

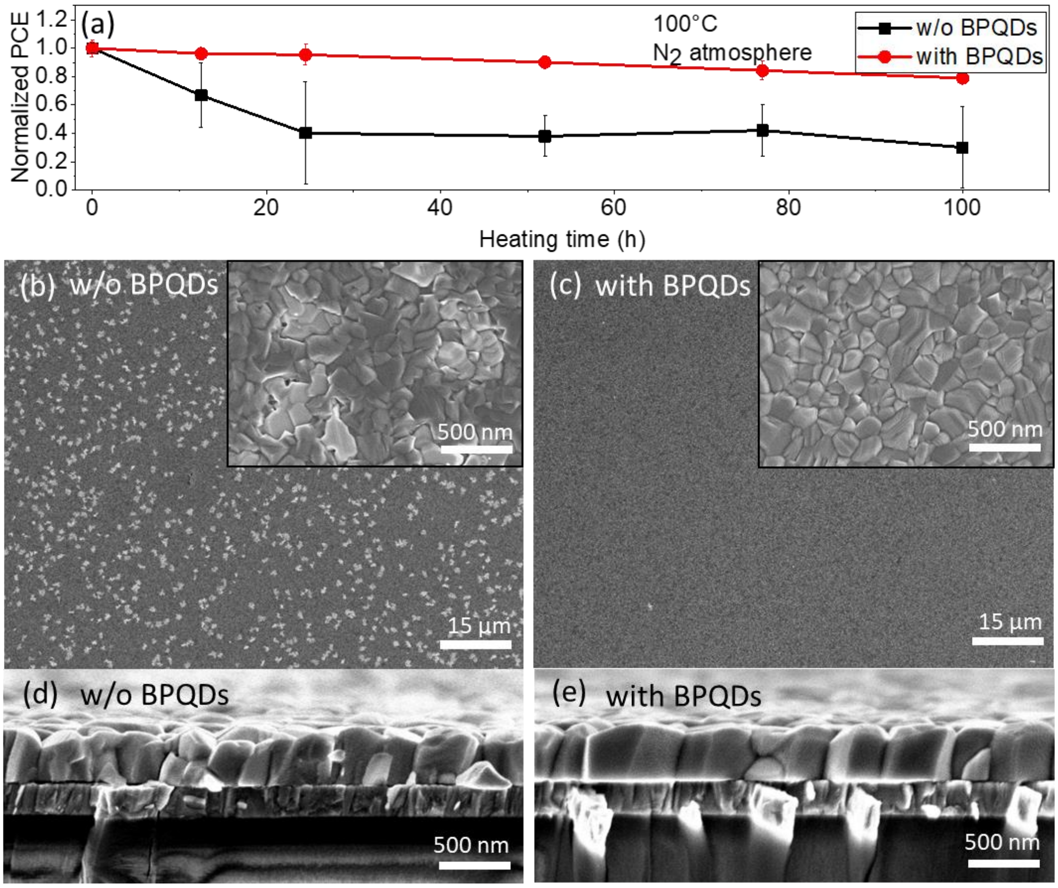

Figure 5. (a) Thermal stability evolution of the unsealed PVSCs heated at 100°C in glovebox. Top-view SEM images of (b) BPQDs-free perovskite film and (c) BPQDs-doped perovskite film after thermal annealing at 100°C for 50 h. Cross-sectional SEM images of (d) BPQDs-free perovskite film and (e) BPQDs-doped perovskite film after thermal annealing at 100°C for 50 h.

Table 1. Photovoltaic parameters of different PVSCs under the illumination of AM 1.5 G, 100 mW/cm^2. The average values are calculated from 24 devices.

additive		V_{OC} (V)	J_{SC} (mA/cm^2)	$J_{cal.}$ (mA/cm^2)	FF	FF_{ave}	PCE (%)	PCE_{ave} (%)
w/o BPQDs	Forward	1.08	21.0	19.8	0.72	0.76±0.02	16.1	16.9±1.0
	Reverse	1.08	21.2		0.78		17.7	
with BPQDs	Forward	1.09	21.6	20.9	0.78	0.80±0.02	18.3	18.7±0.5
	Reverse	1.10	21.9		0.83		20.0	

Black phosphorus quantum dots (BPQDs) assisted growth of perovskite film is reported. Severing as heterogeneous nucleation centers, the BPQDs assist in the crystallization of perovskite film, achieving perovskite films with higher crystallinity and lower non-radiative defects. As a result, perovskite solar cells made with BPQDs achieve a maximum power conversion efficiency of 20% and an encouraging improved thermal stability.

Perovskite Solar Cells

Weitao Yang, Jiehuan Chen, Xiaomei Lian, Jun Li, Fenfa Yao, Gang Wu, Weiming Qiu, Chuanhong Jin, Paul Heremans, and Hongzheng Chen*

Black Phosphorus Quantum Dots Induced High-Quality Perovskite Film for Efficient and Thermally Stable Planar Perovskite Solar Cells

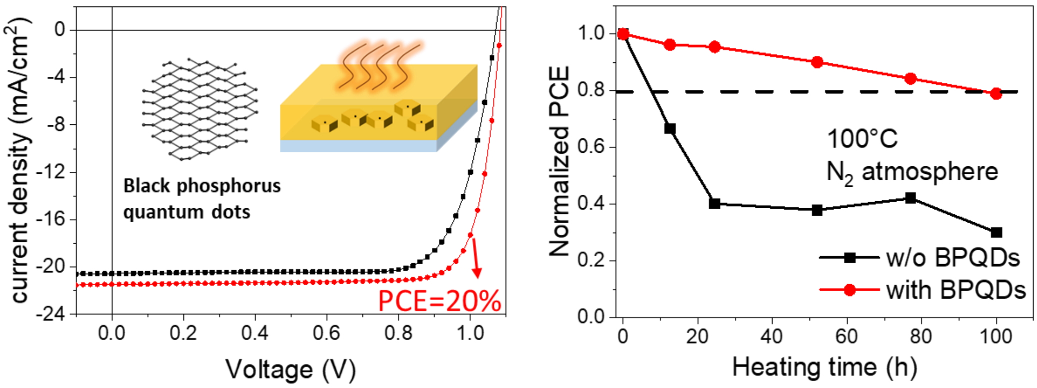

Supporting Information

Black Phosphorus Quantum Dots Induced High-Quality Perovskite Film for Efficient and Thermally Stable Planar Perovskite Solar Cells

*Weitao Yang, Jiehuan Chen, Xiaomei Lian, Jun Li, Fenfa Yao, Gang Wu, Weiming Qiu, Chuanhong Jin, Paul Heremans, and Hongzheng Chen**

Surface density of the BPQDs in perovskite films:

Assuming that the concentration of BPQDs in pervskite film is the same as that of the BPQDs suspension, the number of BPQDs (n) in certain volume (V) could be determined as:

$$\mathrm{n} = \frac{cV}{\rho V_m} \tag{1}$$

Consideing that $V = \mathrm{S} \times L$, the surface density: $\sigma = \mathrm{n/S}$, could be reassembled as:

$$\sigma = \frac{cL}{\rho V_m} \tag{2}$$

Substituting $V_\mathrm{m}=\pi\varphi^2 d/4$, and each constants in the Equation (2), we get $\sigma = 2.9\times10^8$ cm^{-2}.

It’s worth noted that when the nucleation of $\mathrm{MAPbI_3}$ is solely triggered by BPQDs, actually, the grain size of perovskite film will be lager than the calculated inter-QD spacing due to two reasons: i) there would be multiple QDs in a single grain, ii) the loss of BPQDs during the spin-coating process is unaviodable. However, this approximation (underestimatation) wouldn’t conflict with the conclusion we made.

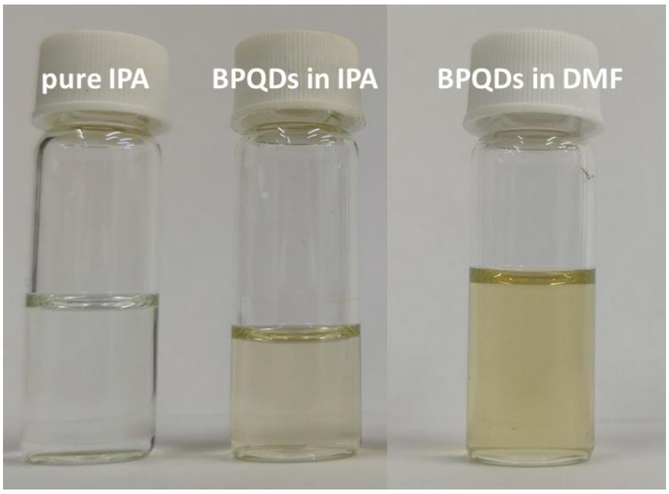

Figure S1. Pure IPA (left), BPQDs suspension in IPA (middle) and in DMF (right). They stay clear and stable for more than 9 months.

Table S1. Photovoltaic parameters of PVSCs with different amounts of BPQD in $MAPbI_3$ under the illumination of AM 1.5 G, 100 mW/cm^2.

Amount of BPQDs$^{a]}$	V_{OC} (V)	J_{SC} (mA/cm^2)	*FF*	PCE (%)
0%	1.08	21.2	0.78	17.7
10%	1.09	21.0	0.80	17.9
25%	1.10	21.6	0.83	20.0
50%	1.09	21.9	0.79	18.4

$^{a)}$The amounts of BPQDs are deterimed by the volume fraction of the BPQDs suspension in the total solution.

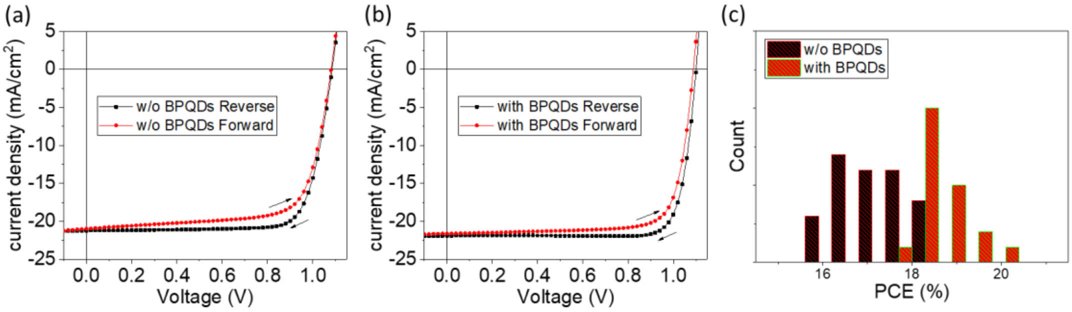

Figure S2. Forward and reverse scanned *J*-*V* curves of the best PVSCs under 1 sun illumination (a) without BPQDs and (b) with BPQDs. (c) The statistics of PCE distribution for devices without and with BPQDs.

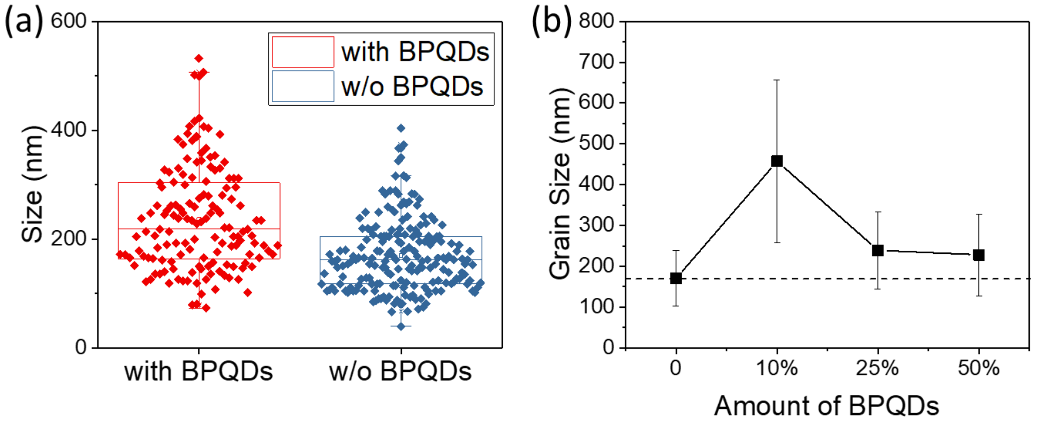

Figure S3. (a) Grain sizes distributions of perovskite films (red) with and (blue) without BPQDs. (b) Grain sizes of perovskite films with different concentrations of BPQDs.

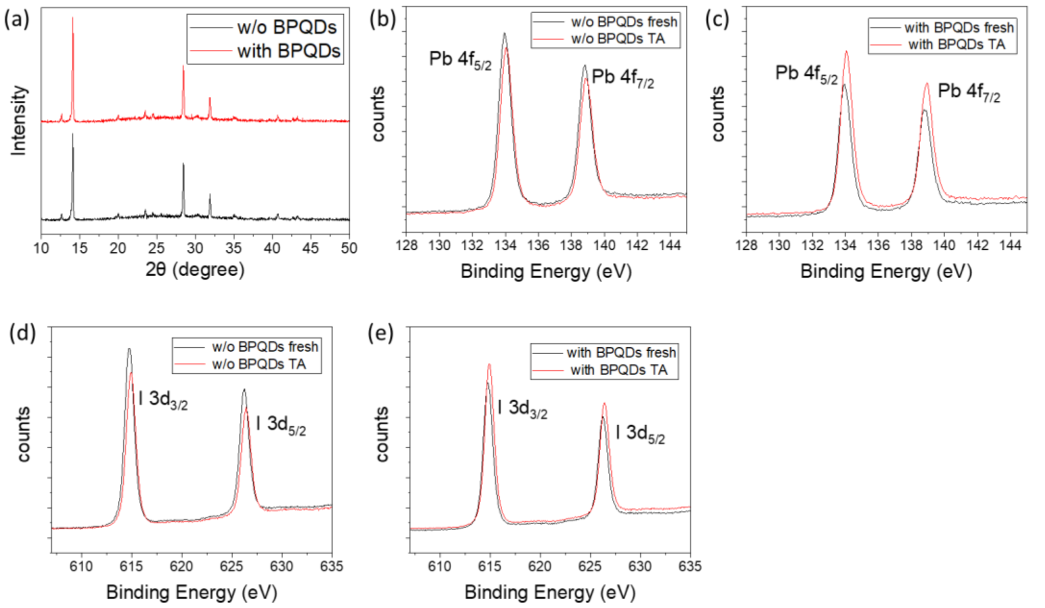

Figure S4. (a) Corresponding XRD patterns of the perovskite films on ITO/PTAA substrate after thermal aging. XPS spectra of (b) Pb 4f and (d) I 3d of perovksite film without BPQDs before and after thermal aging (TA). XPS spectra of (c) Pb 4f and (e) I 3d of perovksite film with BPQDs before and after TA.

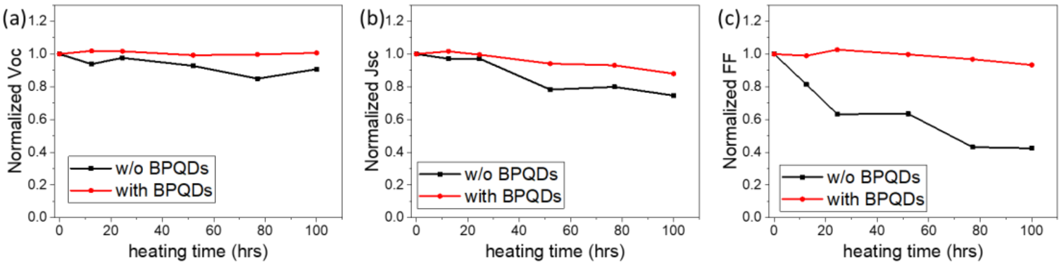

Figure S5. Normalized a) V_{OC}, b) FF, c) J_{SC} of device with (red line) and without (black line) BPQDs under thermal stress at 100°C in nitrogen atmosphere for various times.

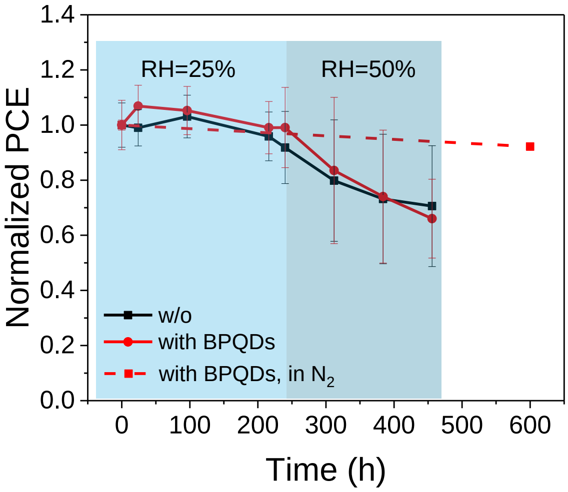

Figure S6. Humidity stability evolution of the unsealed PVSCs stored in ambience with various relative humidity (solid lines). Storage stability evolution of the unsealed PVSCs stored in glovebox.